LAWRENCE
LIVERMORE
NATIONAL
LABORATORY

UCRL-JRNL-215483

Dust-Particle Transport in Tokamak Edge Plasmas

A. Yu. Pigarov, S. I. Krasheninnikov, T. K. Soboleva, T. D. Rognlien

September 19, 2005

Physics of Plasmas

Disclaimer

Dust-particle transport in tokamak edge plasmas

A.Yu. Pigarov[(a),(b)], S.I. Krasheninnikov

University of California at San Diego, La Jolla, California 92093, USA

T.K. Soboleva[(b)]

UNAM, Mexico, D.F., Mexico

T.D. Rognlien

Lawrence Livermore National Laboratory, Livermore, California, USA

a) Corresponding author: apigarov@ucsd.edu (A. Yu. Pigarov)

b) Also with RRC Kurchatov Institute, Moscow 123132, Russian Federation

Abstract

Dust particulates in the size range of 10nm–100μm are found in all fusion devices. Such dust can be generated during tokamak operation due to strong plasma/material-surface interactions. Some recent experiments and theoretical estimates indicate that dust particles can provide an important source of impurities in the tokamak plasma. Moreover, dust can be a serious threat to the safety of next-step fusion devices. In this paper, recent experimental observations on dust in fusion devices are reviewed. A physical model for dust transport simulation, and a newly developed code DUSTT, are discussed. The DUSTT code incorporates both dust dynamics due to comprehensive dust-plasma interactions as well as the effects of dust heating, charging, and evaporation. The code tracks test dust particles in realistic plasma backgrounds as provided by edge-plasma transport codes. Results are presented for dust transport in current and next-step tokamaks. The effect of dust on divertor plasma profiles and core plasma contamination is examined.

Introduction

The study of dusty plasmas includes a wide variety of laboratory and astrophysical plasmas that contain small particles of solid matter widely ranging from few nanometers to hundreds of micrometers. These plasmas have been intensively explored (see reviews [1-5] and literature cited therein). The analysis of dusty plasmas combines fundamentals of plasma and atomic physics, innovative experiments and diagnostics, environmental issues, and novel industrial applications. Dust has become an important research area for large-scale fusion plasma experiments to determine the mechanisms of dust production, dust-plasma and dust-surface interactions, dust transport and removal, as well as assessing the impact of dust on plasma performance and safety of fusion devices.

As shown (e.g. in Refs. [5-11]), dust particles of 10 nm – 100 μm in size are unavoidably present in all fusion devices (as well as larger flakes and loose co-deposited layers of a millimeter and more). Routine analysis [6-10] of dust collected after the vent-to-air in many tokamaks and stellarators give insight into dust distributions, characteristics, and total mass. This analysis indicates that dust particles are comprised mainly of the plasma facing component (PFC) materials used in these machines. These particles had irregular shape akin to grains or globules, and the maximal and minimal dimensions of individual particles do not differ substantially [6,7]. Some characteristics of dust collected in DIII-D, Alcator C-Mod, and NSTX tokamaks are given in Table 1. The characteristic size (for example, the diameter of average-mass dust particles described in [11]) is about several micrometers. The average mass-coverage of dust on plasma-facing component (PFC)

surfaces is several mg/m^2 for carbon-lined tokamaks (NSTX and DIII-D), whereas it is around hundred mg/m^2 for metal-lined C-Mod. Dust is intensively produced on shadowed surfaces, e.g., underneath the graphite tiles, and it accumulates in pumping ducts, diagnostic and neutral beam ports, so that the coverage of entire tokamak vessel is usually much larger than the coverage of PFCs. For such small particulates (~1μm), the measured dust inventories (1-100 g in medium-size tokamaks [6-10]) are relatively large, especially taking into account that these dust particles survived the long time associated with vent activities for tokamak entry.

In tokamak experiments, dust particles are routinely detected moving through the chamber volume by various diagnostics during the plasma discharge [12,13] as well as between the discharges [14]. Advanced studies [15] are recently focused on measurements of dust concentrations in different plasma regions during normal operation. Statistical analysis [15] of signals from Rayleigh channels of Thomson scattering system (TSS) in ~200 consecutive discharges on DIII-D show that the dust concentration in the scrape-off layer varied from about 5×10^{-3} cm^{-3} near the wall to about 5×10^{-4} cm^{-3} at the magnetic separatrix to a much higher concentration ~5×10^{-2} cm^{-3} in the divertor plasma regions.

Dust production in the tokamak environment is a consequence of strong plasma-material interactions. The dust generation rate depends on many factors including stored energy, edge plasma parameters, operation mode, PFC material, particle and power loads onto divertor plates, and wall conditioning. Enhanced release of dust is observed after abnormal operational events [5,16,17] like disruptions, “carbon blooms” due to tile

misalignment, sudden vertical displacements, energetic runaway electrons, and even normal transient events such as ELMs [18]. Estimates [19] show that carbon-dust generation rate averaged over the experimental campaign is rather high, about 100 $\mu g/m^2/s$ in JET and 40 $\mu g/m^2/s$ in JT-60. If so, the generated dust particles should be intensively burn up by plasma in order to maintain the measured PFC coverage of several mg/m^2.

Several possible mechanisms of dust production in tokamaks have been identified: flaking of co-deposited layers, blistering, arcing, and brittle destruction [5,20,21]. Dust can be also generated via carbon condensation from the gas phase, agglomeration from supersaturated vapor, and growth from hydrocarbon molecules [5,22]. However, little is known concerning the production rates due to these mechanisms, nor the parametric dependencies of the rates, generation, and accumulation locations, and size and shape distributions.

Experiments on current tokamaks identify the important safety-related issue that dust particulates and co-deposited layers can contain significant amount of deuterium working gas (and tritium in JET, TFTR); up to 40% of the gas introduced into the machine during the experimental campaign [8,20,23]. The role of dust in tritium retention and in-vessel inventory is discussed in Ref. [24].

The plasma-material interactions in the next-step fusion devices like International Thermonuclear Experimental Reactor (ITER) will be much stronger and the quantity of dust generated is expected to be orders of magnitude larger than those found in present tokamaks, since both the stored plasma energy and the discharge duration will be

substantially increased. Some estimates show that the dust generation rate in ITER can be at the level of hundreds kg/year [20,25]. A variety of dust particles can be formed, including radioactive, chemically reactive, and chemically toxic particles. In an accident, a large amount of dust could be mobilized that creates a potentially serious threat to the ITER and public safety [25-27]. The ITER project has set rigorous safety limits including the limits based on chemical reactivity and radiological hazards of the tokamak dust [25-27]. However, there is a possibility that these limits can be reached sometime during normal ITER operation. To assess and ameliorate this possible situation, means should be developed for dust concentration measurements, dust inventory monitoring, and dust removal [28]. Thorough understanding of dust safety limits and control are important parts of the ITER R&D program [29] including the development and validation of simulation capabilities.

Theoretical and computational models of dust production and transport in fusion devices are in the developmental stage. The general issues of dust particle dynamics in the tokamak plasma (e.g. force balance, lifetime, charging of dust, and acceleration by plasma flows) are discussed in Ref. [30]. Simple stand-alone model for dust heating and survival time in plasma is considered in Ref. [31]. Dust charging, momentum exchange, and drag force between dust and background plasma are studied theoretically [32] and with a Particle-in-Cell (PIC) code [33]. The dynamics of dust particles in the tokamak plasma sheath and recycling regions was first studied in Ref. [34] using a simplified geometry and plasma profile models for a tokamak divertor. As shown [30,34], dust particles can be accelerated by plasma flow in the recycling region to large velocities (10-100 m/s), and they can escape the recycling region due to a successive sequence of

collisions with the corrugated surface of the divertor plate, thus moving far from the wall toward the core plasma. However, little attention has been paid so far to the simulation of plasma-surface interactions leading to dust production (although one can expect that relevant multi-scale modeling efforts may come from other research fields, for example, computational chemistry [35]). Recent theoretical estimates [34] and experiments [15,61] indicate that evaporation of dust particles in plasmas results in a significant de-localized source of impurities. This source may have an effect on material deposition as well as core/edge plasma contamination and should be studied self-consistently with edge plasma transport.

The present paper focuses on the study of dust dynamics and transport in realistic 3D tokamak plasma geometry and conditions. The physical model for dust particle transport is described in Section II. The model incorporates both dust dynamics due to plasma-dust and dust-PFCs interactions as well as the effects of dust heating, charging, and ablation. We have developed the DUST Transport (DUSTT) code and discuss the main features and capability of the code in Section III. In section IV, we analyze the dynamics of carbon dust particles in current diverted-plasma tokamaks NSTX and DIII-D. The dust trajectories in the plasma of the planned ITER device are studied in Section V. Estimates of the impact of dust particles on divertor plasma profiles are given in Section VI. Some conclusions are presented in Section VII.

In the paper, we use the following symbols and units: e is the elementary charge, m_e is the electron mass, m_p is the proton mass, $m_{amu}=1.66\times10^{-24}$ g is atomic mass unit, and h, k, σ_{sb} are the commonly used Planck, Boltzmann, and Stefan-Boltzmann constants. The

plasma ion (T_i) and electron (T_e) temperatures are in eV, whereas the dust temperature (T_d) is in degrees of Kelvin. We use CGS units in the electrostatic-related expressions. The Debye shielding length is denoted as $\lambda_D=\{T_e/[4\pi e^2 n_e]\}^{1/2}$, where n_e is the plasma density. The Dirac delta function of argument x is denoted as $\delta(x)$.

II. Model for dust particle transport in tokamak plasma.

We consider the main forces acting on dust particle, proper account of toroidal geometry, simulation of dust interactions with material surfaces and plasma micro-turbulences, and dust sources. The dust parameters depend strongly on plasma particle and energy fluxes and the model to calculate these fluxes as well as the dust charging will be described. The dust ablation model including thermo-chemical properties and the equations for temporal evolution of dust temperature and size will be discussed.

Dust particle parameters

For simplicity, we assume that the dust particle is spherical with radius R_d. The initial radius R_{d0} of dust particle is an important input parameter. It is also assumed that dust is comprised of uniform solid matter. Then, the total mass M_d and the volume Ω_d of dust particle are functions of radius:

$$\Omega_d=4/3\ \pi[R_d]^3, \quad M_d=\Omega_d\rho_d, \tag{1}$$

where ρ_d is the average mass density. We assume ρ_d be a constant input parameter (neglecting small changes due to dust heating to sublimation temperatures). The dust cross-section area is $\sigma_d=\pi[R_d]^2$ and the surface area is $A_d=4\sigma_d$.

In the multi-phase state, the dust particle enthalpy is

$$H_d=M_d(C_{pd}T_d+\psi_m h_m), \quad (2)$$

where C_{pd} is the heat capacity, ψ_m is the fraction of dust material in the liquid phase, and h_m is the latent heat for melting.

Exact thermo-chemical properties of dust matter in tokamaks are not well known. Here, we assume that the dust particle has the same basic properties as the originating PFC material, including mass density ρ_d, average atomic mass m_d, thermal conductivity κ_d, h_m and C_{pd}, black body (BB) emissivity ε_d, saturated vapor pressure parameters, and melting point temperature T_m.

The NSTX and DIII-D tokamaks considered in Sec. IV are carbon-lined machines, and the collected dust is mainly carbon. Carbon is also the present baseline design for ITER divertor plates. Correspondingly, all calculations reported here are done for dust comprised of high-density carbon material with ρ_d=2 g/cm^3, $m_d=12m_{amu}$, sublimation temperature T_{sub}=3367 C^o, and BB emissivity ε_d=0.75 (Ref. [36]). Carbon materials exhibit no liquid phase but sublimate at high temperatures. The temperature dependence of C_{pd} and κ_d as given in Ref. [37] is used with the inclusion of the sharp increase in C_{pd} for $T_d>T_{sub}$ (Ref. [38]). The heat of thermal sublimation $h_{sub}=2.3\times10^4$ kJ/kg, suggesting that ejection of C_3 clusters dominate this process [39]. Results of calculations for metallic dust particles will be presented elsewhere.

The number of particles in the dust is $N_d=\rho_d\Omega_d/m_d$. So, 1-μm dust particle contains $N_d\approx4\times10^{11}$ cm^{-3} carbon atoms. The hydrogen particle fluxes to dust surface in the tokamak edge plasma can have large values of $\Phi_p\sim10^{20}$ $cm^{-2}s^{-1}$, and the characteristic stopping length λ_{stp} for incident particles in solid matter is about 1 nm. Then, the hydrogen concentration in the surface layer of width λ_{stp} will reach a saturation level $G_{hd}\equiv[H]/[C]$, $G_{hd}=1$, during the time $\tau_{ss}=G_{hd}\rho_d\lambda_{stp}/\{\Phi_p m_d(1-R_N)\}$, where R_N is the particle backscattering coefficient. For $\lambda_{stp}=1$ nm, $R_N=0.5$, one obtains $\tau_{ss}\approx10^{-4}$ s, i.e. τ_{ss} is much smaller than the dust particle residence time $\tau_{dp}\sim10^{-2}$ s in the plasma. Under a saturation condition, the fraction η_r of the hydrogen flux $\Phi_p(1-R_N)$ trapped in the layer will be released back to plasma, whereas the fraction $(1-\eta_r)$ diffuses into the bulk. It is expected that at high surface temperatures the hydrogen release from dust dominates. An upper estimate of the hydrogen content increment, δG_{hd}, is $\delta G_{hd}=\Phi_p A_d(1-R_N)(1-\eta_r)\tau_{dp}/N_d$, where we assume that the dust is filled by $1-\eta_r$ fraction of the trapped flux. For 1-μm dust, $\Phi_p=10^{20}$ $cm^{-2}s^{-1}$, and $\eta_r=0.9$, one obtains $\delta G_{hd}\approx0.02$. There is large uncertainty in the initial hydrogen content. If dust originates from co-deposited layers, then one can expect $G_{hd}=0.1$-0.7 (such hydrogen concentrations in the carbon co-deposited layers were reported in several tokamaks [20]). Thus, except for small dust radii (<100nm), hydrogen concentration in the bulk should not change substantially while dust is traveling in plasma.

Dust electric charge

When the dust surface has no charged-particle emission, we employ the Orbital Motion Limited (OML) model for dust surface charging [40]. In the OML framework, the floating potential φ of a surface is determined by the equality (i.e., ambipolarity condition) of the electron collection current J_e to the ion current on a sphere [41], J_i, where

$$J_e = ¼\, n_{e\infty}[8T_e/(\pi m_e)]^{1/2}\exp(e\varphi/T_e)A_d e, \tag{3}$$

$$J_i = n_{i\infty}[2T_i/m_i]^{1/2}\, F_\Gamma(u,\chi/\delta_{tite})\sigma_d e. \tag{4}$$

Here $n_{e\infty}$, $n_{i\infty}$, and $v_{i\infty}$ are the unperturbed electron and ion densities and plasma flow velocity far from the particle, m_i is the ion mass, $u=v_{i\infty}/[2T_i/m_i]^{1/2}$, $\delta_{tite}=T_i/T_e$, $-e\varphi=\chi T_e$, $F_\Gamma(u,\chi/\delta_{tite})=\{[u+[2u]^{-1}+[\chi/\delta_{tite}]/u]\mathrm{erf}(u)+[\pi]^{-1/2}\exp(-u^2)\}$, and erf(x) is the error function. In deriving Eq. (3-4), it is assumed that: (i) the potential is attractive $\varphi<0$ and cylindrically symmetric, (ii) plasma ions are singly ionized particles, and (iii) $n_{e\infty}=n_{i\infty}$. The floating potential is determined by the following transcendental equation

$$e\varphi/T_e = -\chi = ½\ln|[m_e/m_i]\delta_{tite}| + \ln|\xi_\sigma F_\Gamma(u,\chi/\delta_{tite})|, \tag{5}$$

where $\xi_\sigma = ½[\pi]^{1/2}[4\sigma_d/A_d]$.

Due to ambipolarity of the plasma flux to dust surface, the dust particles develop a negative charge, $-eZ_d$. The dust concentration n_d is considered small, obeying $Z_d n_d << n_e$. The charge number Z_d can be obtained from the relation:

$$e^2 Z_d/R_d = \chi T_e. \tag{6}$$

This relation can be understood as follows: the charge of a conducting sphere obeys the law $eZ_d = C_\varphi\varphi$, where $\chi T_e = -e\varphi$ is the surface potential, and the electrostatic capacitance per unit area for a sphere is $C_\varphi = R_d$.

The dust charge, as well as the friction force between dust and ion (or neutral) particles, can also depend on the shape of dust particle. The effect of dust-particle shapes (e.g. different ratios of dust size vs. the plasma shielding length) is studied in Ref. [42] using the PIC approach and shown to be important. However, the proper incorporation of shape effects requires substantial detail in the dust transport problem (e.g. the description of motion and shape evolution of 3D objects), which is beyond of the scope of the present paper.

The assumption that dust surface does not emit charged particles has some limitations. Under some plasma conditions, especially given the uncertainty in the emission data, a more general model introduces an uncertainty in the value, and even sign, of dust charge and floating potential. In the emission case, the balance of charge particle fluxes at the surface is $J_e=J_i+J_{e,ph}+J_{e,sem}-J_{e,sim}+J_{e,them}$, where $J_{e,ph}$ is the electron flux due to photoemission; $J_{e,sem}$, $J_{e,sim}$ and $J_{e,them}$ are the particle fluxes associated with secondary electron emission from electrons and ions, and the thermal electron emission. Secondary electron emission [41] depends strongly on the flux and energy of incident particles, whereas thermal emission depends crucially on surface temperature and properties of solid material as given by Richardson-Dushman formula

$$J_{e,them}=A_d P_{sb}\{4\pi e m_e[kT_d]^2/h^3\}\exp(-A_w/[kT_d]). \quad (7)$$

Here A_w is the work function, $P_{sb}(T_d)$ is the potential-barrier penetration factor [43]. For high dust temperatures ($T_d>3500C^o$), thermal electron emission can dominate, resulting in a positive charging of the particle surface (assuming $A_w=4.6$ eV, $P_{sb}\approx 0.25$ as for

graphite). The resulting higher flux of hot electrons enhances the heating of the dust. The effects of magnetic field and space charge are expected to be important. A comprehensive model for plasma sheath and corresponding friction force has to be developed to handle this case, which we intend to address in the future.

Equations of motion

The dynamics of test dust particles in a plasma is governed by a set of coupled differential equations for the evolution of radius **r** and velocity **v**, both being 3D vectors. These equations of motion are as follows:

$$d\mathbf{r}/dt = \mathbf{v}, \tag{8}$$

$$M_d(t)\, d\mathbf{v}/dt = \mathbf{F}_d + \Theta_{d,wall}\bullet\mathbf{v} + \Theta_{d,turb}\bullet\mathbf{v}, \tag{9}$$

where $\mathbf{F}_d(\mathbf{r}(t),\mathbf{v}(t),T_d(t),R_d(t))$ is the vector of force applied to a dust particle by the plasma. Operators $\Theta_{d,wall}$ and $\Theta_{d,turb}$ describe, respectively, the collisions of dust particles with material surfaces and with plasma micro-turbulence. The operators have the form

$$\Theta_d = \int\ldots\int d\mathbf{r}d\upsilon d\upsilon' \sum_{k=1}^{k=Kst} \delta(\mathbf{r}-\mathbf{r}_k)\delta_\upsilon(\upsilon_k,\upsilon'_k) \tag{10}$$

where index k runs over a set of collision points, K_{st} is the maximal number of collision points on the trajectory, $\mathbf{r}_k$ is the radius of the collision point, and the parameters $\upsilon\equiv\{\mathbf{v}_k, R_{dk}, T_{dk}\}$ and $\upsilon'\equiv\{\mathbf{v'}_k, R'_{dk}, T'_{dk}\}$ denote velocity, radius, and temperature before and after the collision, $\delta_\upsilon(\upsilon,\upsilon')=\delta(\mathbf{v}-\mathbf{v}_k)\,\delta(\mathbf{v'}-\mathbf{v'}_k)\,\delta(R_d-R_{dk})\,\delta(R'_d-R'_{dk})\,\delta(T_d-T_{dk})\,\delta(T'_d-T'_{dk})$.

To account for the toroidal symmetry of tokamak plasma, we solve the equations using the special coordinate system {r, z, θ}, where r and z are the radial and vertical

coordinates, and θ is the toroidal angle, having the orthogonal basis vectors $\{\mathbf{e}_r, \mathbf{e}_z, \mathbf{e}_\theta\}$. The velocity of dust particle is $\mathbf{v}=v_r\mathbf{e}_r+v_z\mathbf{e}_z+v_\theta\mathbf{e}_\theta$, where v_r, v_z, v_θ are the corresponding velocity components. Thus, one can write Eq. (9) as:

$$dv_r/dt=[v_\theta]^2/r+F_r/M_d, \tag{11}$$

$$dv_z/dt=F_z/M_d, \tag{12}$$

$$dv_\theta/dt=-v_\theta v_r/r+F_\theta/M_d, \tag{13}$$

where F_r, F_z, F_θ are the components of force vector $\mathbf{F}_d$. Equation (8) for radius-vector $\mathbf{r}$ splits into the corresponding set of equations:

$$dr/dt=v_r,\ dz/dt=v_z,\ d\theta/dt=v_\theta/r. \tag{14}$$

The resulting force acting on a dust particle is the vector sum,

$$\mathbf{F}_d=\mathbf{F}_{fric,i}+\mathbf{F}_{fric,n}+\mathbf{F}_E+\mathbf{F}_g, \tag{15}$$

With the plasma/dust friction force $\mathbf{F}_{fric,i}$, neutral/dust friction force $\mathbf{F}_{fric,n}$, electric force $\mathbf{F}_E$, and gravity force $\mathbf{F}_g$. The following expressions are used to calculate the forces:

$$\mathbf{F}_{fric,i}=\xi_i\zeta_{fric,i}m_in_iv_{Ti}(\mathbf{V}_i-\mathbf{v})\sigma_d, \tag{16}$$

$$\mathbf{F}_{fric,n}=\xi_n\zeta_{fric,n}m_nn_nv_{Tn}(\mathbf{V}_n-\mathbf{v})\sigma_d, \tag{17}$$

$$\mathbf{F}_E=-eZ_d\xi_E\mathbf{E}_{plasma}, \tag{18}$$

$$\mathbf{F}_g=M_d\mathbf{g}, \tag{19}$$

where $(m_i, n_i, \mathbf{V}_i)$ and $(m_n, n_n, \mathbf{V}_n)$ are the mass, density, and flow-velocity vector of plasma ions and neutral particles, respectively; the ion and neutral thermal velocities are $v_{Ti}=[2T_i/m_i]^{1/2}$, and $v_{Tn}=[2T_n/m_n]^{1/2}$; $\mathbf{E}_{plasma}$ is the electric field in the plasma; and $\mathbf{g}$ is the gravitational acceleration. Coefficients ξ_i, ξ_n, ξ_E are the scale factors which can be used, for example, to include the change in force magnitude if a particle is non-spherical.

Analytical expressions for the friction force $\mathbf{F}_{fric,i}$ between dust and plasma ion particles are given in Refs. [33,32]. The force has two components: $\mathbf{F}_{fric,i}=\mathbf{F}_{coll}+\mathbf{F}_{orb}$, where $\mathbf{F}_{coll}$ is due to the collection of ions by the dust particle, and $\mathbf{F}_{orb}$ is due to Coulomb scattering. For a negatively charged sphere, the first component is $\mathbf{F}_{coll}=\mathbf{F}_{epstein}T_i/[m_i u^3\pi^{1/2}]$ $\{u[2u^2+1+2\chi/\delta_{tite}]\exp(-u^2)+\pi^{1/2}[4u^4+2u^2-1-2(1-2u^2)\chi/\delta_{tite}]\mathrm{erf}(u)/2\}$, $u=|\mathbf{V}_i-\mathbf{v}|/v_{Ti}$, $\mathbf{F}_{epstein}=m_i n_i v_{Ti}(\mathbf{V}_i-\mathbf{v})\sigma_d$. The second component has the form: $\mathbf{F}_{orb}=\mathbf{F}_{epst}[\chi/\delta_{tite}]^2[\ln\Lambda]\Upsilon(u)/u$, where $\Upsilon(u)=\{\mathrm{erf}(u)-2u\pi^{-1/2}\exp(-u^2)\}/[2u^2]$ is the Chandrasekhar function; the Coulomb logarithm is $\ln\Lambda=½\ \ln\{([b_{90}]^2+[\eta_{fit}\lambda_s]^2)/([b_{90}]^2+[R_d]^2)\}$; $b_{90}=R_d\chi T_i/\{\delta_{tite}m_i[v_{eff}]^2\}$ is the impact parameter, $m_i[v_{eff}]^2=T_i[3+2u^2]$; $[\lambda_s]^{-2}=[\lambda_D]^{-2}\{1+3T_e/(m_i[v_{eff}]^2)\}$ is the screening length, λ_D is the electron Debye radius. We introduce parameter $\eta_{fit}=1+[R_d/\lambda_s]\{1+[T_e/(6T_i)]^{1/2}\}$ in order to accurately fit PIC data from Ref. [32]. We incorporate these expressions in the modified Epstein's form given by Eq. (16) in which the friction coefficient $\zeta_{fric,i}$ is a function of various plasma and dust parameters. The analysis of sensitivity of dust particle dynamics to different model assumptions for the ion friction force will be reported elsewhere.

The dust/neutral friction force $\mathbf{F}_{fric,n}$ has been evaluated in Ref. [44] assuming a constant hard-sphere collision cross-section and Maxwellian distribution of neutrals. In this case, the coefficient $\zeta_{fric,n}$ in Epstein's expression (17) takes the form: $\zeta_{fric,n}=\{(1+s^2-[2s]^{-2})\mathrm{erf}(s)$ $+(s+[2s]^{-1})\exp\{-s^2\}/\pi^{1/2}\}/s$, where $s=|\mathbf{V}_n-\mathbf{v}|/v_{T,n}$.

Dust particle collisions with material surface

When a negatively charged dust particle has a velocity $v>v_*$, $M_d[v_*]^2/2>Z_dT_{e,sheath}$ (v_* is about few m/s for $T_{e,sheath}\approx 10$ eV, $R_d=1$ μm) toward the surface, the particle has enough energy to overcome the electrostatic sheath barrier, and collide with the material surface. However, experimental data on dust particle reflectivity from the material surface is lacking.

To describe the reflectivity of dust particle from material surfaces, we introduce effective coefficients for dust mass, temperature, and velocity reflection, and employ a simple diffusive-mirror reflection model for velocity vector. The mass reflection coefficient is $P_{ref,m}=R_d'/R_d$, $0\le P_{ref,m}\le 1$, where R_d and R_d' are the dust radii before and after the wall collision, so that the fractional dust mass loss per collision is equal to $[P_{ref,m}]^3$. Similarly, the dust temperature reflection coefficient is $P_{ref,T}=T_d'/T_d$. The velocity reflection coefficient is $P_{ref,v}=|\mathbf{v}'|/|\mathbf{v}|$, $0\le P_{ref,v}\le 1$, where $|\mathbf{v}'|$ and $|\mathbf{v}|$ are the velocity magnitudes after and before collision. In analogy to atomic particle reflectivity [50,51], the dust reflection coefficients can also be generalized to depend on incident energy and angle.

Consider the Cartesian coordinate system with the origin at the point of dust collision with the material surface. The vector **n** denotes the unity normal vector, so that $\mathbf{v}\cdot\mathbf{n}<0$ corresponds to being directed toward the plasma. The incident dust flux is $F_{(+)}=M_d\, n_d\, |\mathbf{v}\cdot\mathbf{n}|$, where n_d is the dust number density in the incident ray. The **v**' distribution of reflected dust particles, Φ, has the following form:

$$\Phi(\mathbf{v}\rightarrow\mathbf{v}')=p_{dif}\,\Phi_{dif}(\mathbf{n},\mathbf{v}')+(1-p_{dif})\Phi_{mir}(\mathbf{v},\mathbf{n},\mathbf{v}'), \quad (20)$$

which is normalized to the reflected flux $F_{(-)}=F_{(+)}[P_{ref,m}]^3P_{ref,v}$, that is, $\int_{\{\mathbf{v}'\mathbf{n}>0\}}\Phi(\mathbf{v}\rightarrow\mathbf{v}')d\mathbf{v}'=F_{(-)}$, where p_{dif}, $0\le p_{dif}\le 1$, denotes the probability of diffusive reflection. The $\mathbf{v}'$ distribution function for mirror reflection is $\Phi_{mir}(\mathbf{v},\mathbf{n},\mathbf{v}')=\delta(\mathbf{v}'-P_{ref,v}\{\mathbf{v}-2\mathbf{n}(\mathbf{n}\times\mathbf{v})\})$. For diffusive reflection, the corresponding distribution function is isotropic, i.e., $\Phi_{dif}(\mathbf{n},\mathbf{v}')=\delta(|\mathbf{v}'|-P_{ref,v}\cdot|\mathbf{v}|)\cdot|\mathbf{v}'\cdot\mathbf{n}|$.

Dust particle collisions with plasma micro-turbulence

As shown [45-47], anomalous cross-field plasma transport in the scrape-off layer (SOL) of tokamaks is not purely diffusive but also convective due to intermittent coherent structures, the so-called blobs (referring to their shape on the poloidal cross-section). In a simple picture of convective intermittent transport, blobs originate in the core plasma near the separatrix and move with a nearly ballistic trajectory across the SOL. As measured [46,47], blobs have characteristic radii R_b~1 cm and cross-field velocities $V_{cf,b}\sim 10^5$ cm/s. The plasma carried by the blob has density N_b and temperature T_b much higher than the average plasma density in the SOL. The dust collision with blob, $\tau_b=2R_b/V_{cf,b}\sim 2\times10^{-5}$ s, is fast compared to dust transport times (~10^{-3} s), so we treat dust-blob interactions as a scattering events.

In edge plasma physics codes, the effect of blobby cross-field transport is modeled by introducing the 2D profile of convective velocity V_{conv} (see Ref. [48], for details). This profile is adjusted to match experimental data. The plasma flux n_eV_{conv} carried by blobs is

calculated by the code. The averaged frequency f_b of blobs can be determined from particle balance: $N_b V_{cf,b} \tau_b f_b = n_e V_{conv}$. The mean free path length (MFPL), λ_{db}, for dust/blob collisions has Gaussian distribution, $p_\lambda(\lambda_{db}) \propto \exp\{-[\lambda_{db}/\lambda_*]^2\}$, where $\lambda_* = v_d/f_b$ is the average MFPL, and v_d is the dust velocity.

In our model, the velocity distribution function (VDF) of scattered dust particles, $\Phi_{sct}(\mathbf{v} \rightarrow \mathbf{v}')$, is the weighted sum of delta-scattering (Φ_δ) and scaled blob velocity (Φ_b) VDFs:

$$\Phi_{sct}(\mathbf{v} \rightarrow \mathbf{v}') = p_\delta \Phi_\delta(\mathbf{v},\mathbf{v}') + (1 - p_\delta)\Phi_b(\mathbf{v}_b,\mathbf{v}'), \quad (21)$$

where $\mathbf{v}$ and $\mathbf{v}'$ are the velocities before and after the collision, p_δ is the probability of fictitious scattering without change in the velocity vector, $\Phi_\delta = \delta(\mathbf{v}' - \mathbf{v})$. The VDF of dust captured by blob is $\Phi_b = \delta(\mathbf{v}' - P_{db,v} \cdot \mathbf{v}_b)$, where $P_{db,v}$ is the scale factor, and the components of blob velocity vector $\mathbf{v}_b$ are: $v_{br} = V_{cf,b} \mathbf{h}_\perp \mathbf{e}_r$, $v_{bz} = V_{cf,b} \mathbf{h}_\perp \mathbf{e}_z$, $v_{b\theta} = M_b v_{Tb}$, $v_{Tb} = [2T_b/m_i]^{1/2}$, M_b is the Mach number for parallel plasma flow in the blob, and $\mathbf{h}_\perp$ is unity vector normal to the magnetic flux surface.

Notice, the dust velocity can change significantly in collision with a blob. While blob is interacting with dust particle, the velocity increment due to ion friction force is $\delta v_d = \tau_b F_{fric,i}/M_d = \tau_b \xi_i \zeta_{fric,i} m_i N_b [v_{Tb}]^2 M_b \sigma_d / M_d$. For $\tau_b = 2\times10^{-5}$ s, $m_i = 2m_{amu}$, $\xi_i = 1.5$, $\zeta_{fric,i} = 10$, $M_b = 0.3$, $R_d = 1$ μm, $T_b = 200$ eV, $N_b = 2\times10^{13}$ cm^{-3}, the velocity increment in toroidal direction is $\delta v_d \approx 0.5\times10^4$ cm/s that is close to the cruise velocity of dust particle ~$(1\text{-}2)\times10^4$ cm/s. The factor $P_{db,v}$ is of order $\delta v_d/\{v_{Tb} M_b\} \approx 10^{-3}$. The increment increases with

decrease in dust radius as $\propto 1/R_d$. For $p_\delta<1$, the dust scattering by blobs introduces some randomness to the dust trajectory in plasma.

Ablation model for dust particles

The surface of dust particle in plasma is intensively bombarded by: (i) plasma electrons, (ii) hydrogen isotope ions and neutral atoms, (iii) impurity ions in various charge states and impurity atoms, and (iv) photons. Interactions of all these particles with dust matter results in net erosion and mass loss for a dust particle. Moreover, the heat flux associated with kinetic energy exchange, release of plasma potential energy, and absorption of radiation is capable of heating the dust particle up to the melting and sublimation temperatures causing the phase change in matter and enhanced evaporation. The simple model to calculate the particle and heat fluxes associated with incident and ejected particles as well as the characteristic energy of bombarding particles will be discussed in this subsection. The model corresponds to the case when dust surface exhibits no charged particle emission.

In the OML theory framework, the incident hydrogen ion flux $\Gamma_{i,h}$ on the negatively charged sphere is $\Gamma_{i,h}=n_{i,h}v_{i,h}F_\Gamma(u,\chi/\delta_{tite})\sigma_d/A_d$, where $n_{i,h}$ is the proton density, $v_{i,h}=[2T_i/m_h]^{1/2}$. Taking into account ion acceleration in the electrostatic sheath potential (χ), the energy of protons arriving at the surface is $E_{i,h}=\zeta_i T_i+\chi T_e$, where ζ_i is the ion energy sheath transmission coefficient; $\zeta_i=2.5$ corresponds to Maxwellian ion VDF drifting with speed $v_{i,h}$. There is no reliable model describing multi-species transport of

impurities ions in the sheath. For simplicity, we assume the impurity ion flux is $\Gamma_z=n_z v_{i,z}$, where index z denotes the charge state of ion, n_z is the density of z-ions, and $v_{i,z}=[2T_z/m_z]^{1/2}$. The energy of impurity ions is $E_z=\zeta_z T_z+z\chi T_e$. The fluxes of neutral hydrogen ($\Gamma_{a,h}$) and impurity ($\Gamma_{a,imp}$) atoms are $\Gamma_{a,h}=¼\ n_{a,h}v_{th,h}$ and $\Gamma_{a,imp}=¼\ n_{a,imp}v_{th,imp}$. Here the number density, temperature, and mean velocity are given for hydrogen neutral atoms ($n_{a,h}$, $T_{a,h}$, $v_{th,h}=\{8T_{a,h}/[\pi m_h]\}^{1/2}$) and for impurity atoms ($n_{a,imp}$, $T_{a,imp}$, $v_{th,imp}=\{8T_{a,imp}/[\pi m_z]\}^{1/2}$). The averaged energies of neutrals striking the surface are $E_{a,h}=\gamma_a T_{a,h}$, $E_{a,imp}=\gamma_a T_{a,imp}$, and $\gamma_a=2$ for Maxwellian VDF of atoms.

As mentioned, we assume that the hydrogen concentration in the dust surface layer is saturated. Then, the hydrogen particle flux into the dust $\Gamma_{h,in}=\Gamma_{i,h}+\Gamma_{a,h}$ is balanced by the outflux $\Gamma_{h,out}=R_N(E_{i,h},\theta_w)\Gamma_{i,h}+R_N(E_{a,h},\theta_w)\Gamma_{a,h}+G_{detrap}$, where R_N, $0\le R_N\le 1$, is the particle reflection coefficient that determines the backscattering probability, such that $(1-R_N)$ is the probability for particle trapping in the solid matter. This coefficient depends on projectile energy, incident angle, and surface material [50, 51]. The generic term G_{detrap} describes the net release of trapped hydrogen due to thermal emission of atoms and molecules, and sputtering by incident particles.

In fusion devices, both dust and intrinsic impurity atomic particles have the same origin from plasma facing components. Thus, we assume that impurity ions and atoms correspond to the same elements as the dust particles. The total flux of impurity ions into dust is

$$\Gamma_{imp,in}=\Sigma_z\Gamma_z+\Gamma_{a,imp}, \tag{22}$$

whereas the flux of particles emanating from the dust is

$$\Gamma_{imp,out}=\Gamma_{refl}+\Gamma_{phy}+\xi_{ch}\Gamma_{ch}+\xi_{RES}\Gamma_{RES}+\xi_{sub}\Gamma_{sub} \quad (23)$$

with contributions from impurity particle reflectivity (Γ_{refl}), physical (Γ_{phy}) and chemical (Γ_{ch}) sputtering, as well as radiation-enhanced (Γ_{RES}) and thermal (Γ_{sub}) sublimations. The components of $\Gamma_{imp,out}$ have the following form: $\Gamma_{refl}=\Sigma_z R_N(E_z,\theta_w)\Gamma_z+R_N(E_{a,imp},\theta_w)\Gamma_{a,imp}$, $\Gamma_{phy}=Y_{phy}(E_{i,h},\theta_w)\Gamma_{i,h}+\Sigma_z Y_{phy}(E_z,\theta_w)\Gamma_z+Y_{phy}(E_{a,h},\theta_w)\Gamma_{a,h}+Y_{phy}(E_{a,imp},\theta_w)\Gamma_{a,imp}$, $\Gamma_{ch}=Y_{ch}(E_{i,h},\theta_w,T_d,\Gamma_{tot})\Gamma_{i,h}+Y_{ch}(E_{a,h},\theta_w,T_d,\Gamma_{tot})\Gamma_{a,h}$, where Σ_z denotes the summation over z, $\Gamma_{tot}=\Gamma_{imp,in}+\Gamma_{h,in}$ is the total particle flux, and θ_w is an effective angle of incidence [52]. The physical and chemical sputtering processes are represented by sputtering-yield coefficients, Y_{phy} and Y_{ch}. Analytical formulas to calculate the physical sputtering $Y_{phy}(E,\theta)$ is given in Ref. [53]. We also compute the averaged energies of sputtered particles $E_{phy,h}$, $E_{phy,z}$, $E_{phy,a,h}$, and $E_{phy,a,imp}$ associated with incident fluxes $\Gamma_{i,h}$, Γ_z, $\Gamma_{a,h}$, and $\Gamma_{a,imp}$, respectively. These energies are obtained by averaging over the VDF of incident particles and Tompson spectrum, parameters of which implicitly depend on incident energy and angle. The analytical expressions for chemical sputtering yield $Y_{ch}(E,\theta,T,\Gamma)$ as a function of projectile energy, incident angle, surface temperature, and total particle flux for different projectiles and targets are summarized in Ref. [54]. The averaged energy of solid particles ejected by chemical sputtering is $E_{ch}=\zeta_{ch}T_d$, where $\zeta_{ch}=2$ for thermal flux of particles with Maxwellian VDF. Radiation enhanced sublimation observed for some materials (e.g. for C) provides an important mass-loss mechanism at high surface temperatures T_d=1000-2500K. For carbon, analytical expressions for Γ_{RES} flux are given in Ref. [55] and we use them to calculate RES contributions from incident ions and neutrals. For dust temperatures >2500K, thermal

evaporation, Γ_{sub}, is the dominant loss mechanism for dust mass. To calculate Γ_{sub} for carbon dust we use a semi-analytical formula [36]:

$$\Gamma_{sub}=C_{\Gamma}\cdot[M_{c3}/T_d]^{1/2}\exp\{[B-A/T_d]\cdot b_{10}\}, \quad (24)$$

where Γ_{sub} is in g $cm^{-2}s^{-1}$, $C_{\Gamma}=4.32\times10^{-4}$, $M_{c3}=36$ is the molecular weight of C_3 cluster, A=15.75 and B=40750 are the saturated vapor pressure parameters, $b_{10}=\ln(10)$, and T_d is in degrees of Kelvin. Coefficients ξ_{ch}, ξ_{RES} and ξ_{sub} take into account the fraction of carbon particles ejected as C_xH_y, C_x, x>1, molecules.

Due to interactions with the plasma, the radius R_d of a spherical dust particle decreases in time as follows:

$$\rho_d dR_d/dt=m_d[\Gamma_{imp,in}-\Gamma_{imp,out}]. \quad (25)$$

In obtaining Eq. (25) account is taken of the equality: $dM_d/dt=A_d\rho_d\cdot dR_d/dt$.

The total heat flux q_{plas} applied to the dust surface is

$$q_{plas}=q_{kin,i}+q_{kin,e}+q_{kin,n}+q_{pot}, \quad (26)$$

as due to kinetic energy transfer from plasma ions ($q_{kin,i}$), electrons ($q_{kin,e}$) and neutrals ($q_{kin,neut}$), as well as release of plasma ion potential energy (q_{pot}). We calculate specific heat fluxes as $q_{kin,i}=\Gamma_{i,h}E_{i,h}+\Sigma_z\Gamma_zE_z$, $q_{kin,e}=E_{el}\Gamma_e$, $q_{pot}=I_h\Gamma_{i,h}+\Sigma_z\Gamma_z\{\Sigma_zI_{imp}(z\text{-}1)\}$, $q_{kin,n}=E_{a,h}\Gamma_{a,h}+E_{a,imp}\Gamma_{a,imp}$, where $E_{el}=\{\zeta_e-\chi\}T_e$, $\Gamma_e=\Gamma_{i,h}+\Sigma_z z\Gamma_z$, ζ_e is the electron energy sheath transmission coefficient, I_h and $I_{imp}(z)$ are the ionization potentials of hydrogen and impurity particles, and χ is given by Eqs. (3-5). The total heat flux q_{ejct} associated with kinetic energy of particles ejected from dust is

$$q_{ejct}= q_{refl}+q_{phy}+q_{ch}+q_{RES}+q_{sub}, \quad (27)$$

where $q_{refl}=\Gamma_{i,h}E_{i,h}R_E(E_{i,h},\theta_w)+\Sigma_z E_z\Gamma_z R_E(E_z,\theta_w)+E_{a,h}\Gamma_{a,h}R_E(E_{a,h},\theta_w)+E_{a,imp}\Gamma_{a,imp}R_E(E_{a,imp},\theta_w)$, $q_{phy}=E_{phy,h}Y_{phy}\Gamma_{i,h}+\Sigma_z E_{phy,z}Y_{phy}\Gamma_z+E_{phy,a,h}Y_{phy}\Gamma_{a,h}+E_{phy,a,imp}Y_{phy}\Gamma_{a,imp}$, $q_{ch}=E_{ch}[Y_{ch}\Gamma_{i,h}+Y_{ch}\Gamma_{a,h}]$, $q_{RES}=h_{RES}\Gamma_{RES}$, $q_{sub}=h_{sub}\Gamma_{sub}$, $R_E(E,\theta)$ is the energy reflection coefficient given by Refs. [50, 51], and the specific heat for RES is taken as $h_{RES}=0.78$ eV for carbon.

When heat flux is applied to the dust surface, the temperature profile within the dust can change practically immediately because the particle size is small and heat conduction is fast. In fact, the characteristic time $\tau_{cond}=\rho_d C_{pd}[R_d]^2/\kappa_d$, where κ_d is the thermal conductivity coefficient. For 1-μm carbon dust particle at surface temperature $T_d=1000C^o$, $C_{pd}\approx 1.3$ J/g/C^o, $\kappa_d\approx 1$ W/cm/C^o, the conduction time is about $\tau_{cond}\approx 3\times 10^{-8}$ s that is several orders of magnitude smaller than the dust transport time $\sim 10^{-3}$ s. If the cruise speed is $v_d=100$ m/s, the particle will travel to a distance $v_d\tau_{cond}\approx 3\times 10^{-4}$ cm that is small compared to typical gradients of plasma parameters. These estimates justify our simplified assumption that temperature profile is flat inside the dust particle.

The temporal evolution of dust enthalpy (and, implicitly, of temperature T_d) obeys

$$dH_d/dt=4\pi[R_d]^2 q_{net}, \tag{28}$$

$$q_{net}=q_{plas}-\varepsilon_d\sigma_{sb}\{[T_d]^4-[T_w]^4\}-q_{ejct}, \tag{29}$$

where the second term on the *rhs* of Eq. (29) describe black-body radiation cooling, and T_w is the temperature of tokamak chamber interior surfaces. When dust matter can be in the liquid phase (for example, molybdenum used in Alcator C-Mod and tungsten in ITER), we solve the additional equation:

$$d[M_d h_m \psi_m]/dt = 4\pi [R_d]^2 q_{net}, \quad (30)$$

which will determine the melted fraction ψ_m under condition $T_d = T_m$.

The dust ablation model is thus given by Eqs. (25,28,30) describing the temporal evolution of the dust radius and enthalpy. For our dust particle tracking calculations, the dust radius and temperature also decrease due to collisions with material surfaces and micro-turbulence according to reflection coefficients $P_{ref,m}$ and $P_{ref,T}$, which are not explicitly represented in the equations above for simplicity of presentation.

Source of dust particles

There are two sources of dust in tokamaks: (i) intrinsic dust detached from PFCs, and (ii) injected dust for diagnostic purposes [56]. Here, we report on simulations of intrinsic dust. The mechanisms of dust production and distribution function of intrinsic dust are not yet well understood. Some modeling [57] shows that for dust ejection due to brittle destruction, the particles originate at large velocities ~100 m/s, so they can freely leave the electrostatic plasma sheath region. However, in the cases when dust grows and flakes from co-deposits, the initial dust velocity is expected to be small (< 1m/s) and the ejected particle is likely trapped in the sheath. The processes of dust levitation, collision with irregular and corrugated surfaces, and acceleration in the sheath have been studied in Ref. [30,34]. As shown, dust can be ejected from the sheath and pre-sheath with high velocities up to 10 m/s.

Dust detachment from surfaces and acceleration in the sheath are not simulated here, instead we prescribe the initial dust velocity distribution. The value of initial velocity v_{d0} is important input parameter of our model. We either input or randomly generate the initial values of the particle's polar (μ_{d0}) and azimuthal (ϕ_{d0}) angles at the originating PFC surface. The birth point is typically specified, but it can also be randomly chosen based on the PFC heat load distribution.

Dust break-up

We assume that dust explodes as soon as the slowing-down distance of incident plasma ions (λ_{id}) or electrons (λ_{ed}) in the solid matter becomes comparable to the dust radius. The formulas to calculate λ_{id} and λ_{ed} are given, e.g., in Ref. [58]. In practice, we stop following the particle when dust radius becomes α_{rd} times smaller than the initial radius, or current radius becomes $R_d \leq max\{\lambda_{id},\lambda_{id}\}$, whichever occurs first. There are also specific processes that limit the magnitudes of surface potential and charge of a dust particle. High surface potential can cause electrostatic disruptions [59] of dust. The critical potential φ_* for disruption is estimated as $|\varphi_*|=\beta[F_t]^{1/2}R_d$, where F_t is the tensile strength of material in dyne/cm^2, numerical factor $\beta\approx 0.1$, the dust radius is in μm, and φ_* is in Volts. At the critical potential, the particle is split into two stable fragments radius $R_d'=R_d\gamma_{split}$, $\frac{1}{2}<\gamma_{split}<2^{-1/3}$ (the rest of dust mass, $1-2[\gamma_{split}]^3$, is considered to be sublimated).

III. The DUSTT code

The physical model described in Section II is implemented in the DUST Transport (DUSTT) code. The code thus simulates the 3D transport of test dust particles in realistic tokamak plasma environment.

DUSTT uses input data for the profiles of multi-species plasma and neutral gas parameters, flow velocities, particle and heat fluxes on material surfaces, electric field, as well as the magnetic configuration and tokamak chamber geometry, directly from the edge-plasma transport code UEDGE [60]. UEDGE employs a multi-fluid approach to simulate transport of plasma electrons, ions, neutral atoms, and impurity species. In a series of code runs, the profiles of anomalous cross-field plasma diffusivities and convective velocities are adjusted to match extensive sets of experimental data for the tokamak discharges. In this sense, the plasma background used for dust tracking represents available experimental data.

As does UEDGE, DUSTT operates on 2D curvilinear non-uniform mesh based on reconstruction of tokamak MHD equilibrium for specific plasma discharges. Plasma/neutral parameters are assumed to be constant within a mesh cell and toroidally symmetric.

Between collisions, the dynamics of test dust particle is determined by Newton law equations. The resulting force acting on a dust particle depends strongly on plasma

parameters and flows as well as on dust radius, temperature, and electric charge. In the model, the equations of motion Eqs. (11-14) are coupled to the equations for the dust radius Eq. (25), enthalpy Eqs. (28-30), and charge Eqs. (5-6). We use a simple explicit solver for the system of coupled differential equations. The Monte Carlo method is used to treat the collisions of dust with material surfaces and plasma micro-turbulence, which is widely used to simulate neutral particle transport (see, for example, Ref. [49]). We may also employ the Monte Carlo method in the case when averaging over an ensemble of test dust particles is required. In this case, initial parameters (birth point, velocity vector, mass, radius, etc) are scored using model distribution functions as will be discussed in another paper.

Evaporation of dust particles in plasma results in volumetric sources of impurity atoms and ions. We show that in contrast to other impurity sources due to physical and chemical sputtering by plasma ions and neutrals, where the mean free path of neutral impurity atom/molecule is less than a centimeter, dust particles are capable of traveling a distance of about a meter and penetrating deeply into the plasma. The effect of dust-related distributed impurity sources on plasma profiles should be studied self-consistently, and work on coupling the DUSTT and UEDGE codes is in progress.

Future plans are for DUSTT to incorporate detailed models for dust generation, acceleration in the magnetized plasma sheaths as well as the effects of dust shape and charge particle emission. Improved models for dust transport in edge plasma, collisions

with walls and micro-turbulence, plastic deformation and break-up, and mixed-material ablation are also required.

For the DUSTT code calculations reported here, we use the following values of miscellaneous input parameters of the model. The hydrogen ion and gas masses, m_i and m_h, are $2m_{amu}$ for deuterium working gas (NSTX, DIII-D) and $2.5m_{amu}$ for deuterium-tritium mixture (ITER). Analytical fitting formulas to Hutchinson's data [33] are used in order to calculate the ion/dust friction force coefficient $\zeta_{fric,i}$. The force scale factors are $\xi_i=\xi_n=3/2$, $\xi_E=1$. Since the plasma and gas are multi-species, in computing the ion and neutral friction forces we sum forces from different species and charge states. It is assumed that all ion species and ion charge states have the same temperature $T_z \equiv T_i$. For dust refection from material surfaces, we use $P_{ref,m}=0.95$ and $P_{ref,v}=0.8$, which provide relatively small losses of mass (≈ 0.857) and energy (≈ 0.686) for dust particles, and the pessimistic value $P_{ref,T}=1$. Equal probabilities are used for mirror and diffusive reflection, i.e. $p_{dif}=0.5$. In dust-blob collision model, we take $M_b=0.3$, $V_{cf,b}=10^5$ cm/s, and use small value $1-p_\delta=0.1$ (thus, we reduce the scattering effect here and intend to report detailed study of this effect in the future). In computing the particle and energy fluxes on dust, we use $\zeta_z=\zeta_i=2.5$, $\zeta_e=2.5+\chi$. The trajectory is terminated when the radius $R_d=R_{d0}/\alpha_{rd}$, $\alpha_{rd}=10$.

III. Dust dynamics in NSTX and DIII-D tokamaks

Examples of trajectories of dust particles in a tokamak are shown in Fig.1. These trajectories are calculated by the DUSTT based on the plasma background simulated with

UEDGE by matching the experimental plasma profile data for typical L-mode shot 109033 on NSTX tokamak. On upper panels, we display two 3D plots (in {r, z, θ} space, where r and z are the radial and vertical coordinates, θ is the toroidal angle) for trajectories originating in the strike point on the inner (left upper panel) and outer (right) divertor plates. In both cases: v_{d0}=1 m/s, $\mu_{d0}=30^o$, r_{d0}=1 μm. The trajectories begin at θ=0. The corresponding 2D traces of these trajectories on the UEDGE mesh are shown on the bottom panels. As can be seen on left panels, the particle originates from the inner divertor and initially moves in the vicinity of the divertor plate. The particle collides a few times with the plate and then travels along the private flux region into the outer divertor. After a collision with the outboard side of chamber wall, the particle penetrates close to the X-point and is terminated there owing to mass loss. The trajectory in the right panels of Fig. 1 shows a dust particle in the outer divertor. After several collisions with the outer plate, it moves poloidally almost along the separatrix leg toward the X-point. Both particles are very mobile and travel long distances, >0.5 m poloidally, until mostly evaporated.

The trajectories shown on Fig. 1 are elongated in the toroidal direction, which can be understood by comparing the increments in toroidal length $\delta L_\theta=\int|v_\theta|dt\approx\langle r\rangle*\Delta\theta$ and poloidal length $\delta L_p=\int[v_r^2+v_z^2]^{1/2}dt\approx[\Delta r^2+\Delta z^2]^{1/2}$. In fact, the trajectory starting in the outer divertor (right panels), $\langle r\rangle\approx0.7$, $\Delta r\approx0.2$, $\Delta z\approx0.2$ m, and $\Delta\theta\approx1.3$ has $\delta L_\theta/\delta L_p\approx3$. The trajectory elongation in the θ-direction is confirmed by some experiments. Another important feature is that near the divertor plates the preferential toroidal direction of dust trajectories depends on the direction of parallel plasma flow, which is different near the

inner and outer plates. In Fig.1 (left top), the dust particle moves in the negative θ direction while in the inner divertor, and it reverses its θ direction when reaching the outer divertor. Such behavior is due to the dominance of ion friction force. Comparing left and right top plots, the particles in the recycling regions near divertor plates move in opposite toroidal directions.

Using DUSTT, we also analyzed dust trajectories for L-mode shot 105517 in DIII-D tokamak. The plasma profiles for this shot have been discussed in Ref. [48]. The dust trajectory originated from the outer divertor strike point, v_{d0}=10 m/s, μ_{d0}=30^o, r_{d0}=1 μm, is shown on Fig. 2(a). The total ($L_t=\int_o^t|\mathbf{v}|dt$) and poloidal ($L_p=\int_o^t[v_r^2+v_z^2]^{1/2}dt$) distances traveled by this particle are displayed on panel (b) versus time. The characteristic time this dust particle resides in the plasma is several ms and the maximum traveled distances are $L_{t,max}\approx$1.7 m and $L_{p,max}\approx$0.7 m. The evolution of the dust temperature T_d and the normalized mass M_d/M_{d0} along the trajectory (i.e. along coordinate $L_p/L_{p,max}$) are displayed in the (c) and (d) panels. When the particle travels through the hot and dense regions, it heats up to sublimation level (>2500K) and cools in the weak plasma regions. At low temperatures T_d<2000K, the mass loss is small. The dust mass decreases substantially due to collisions with the PFCs and from combined RES and thermal sublimation. The variations of particle and heat loads applied to the dust surface are shown along the trajectory in the (e) and (h) panels (the fine steps on these curves are due to transitions in the UEDGE mesh). The loads sharply increase when the dust passes through the hot plasma region around the separatrix leg. Comparing the plots for T_d and incident heat flux q_{plas}, one sees that after the "heat pulses" at $L_p/L_{p,max}\approx$0.03, ≈0.11,

≈0.45, and 0.85, the particle is continuously cooling by black-body radiation; however, there is not enough time for this particle to substantially cool before it again encounters the hot plasma upon reflection from the end plate. The velocity magnitude $|\mathbf{v}_d|$ and components are given in the (g) and (h) panels of Fig. 2. The dust particle is accelerated by the plasma to large velocities (v_d>100 m/s). This acceleration takes place mainly in the region near the divertor plate where parallel plasma flow is the largest. The mean speed over most of the trajectory is few hundreds m/s, while at the end of the trajectory, the velocity reaches ~1 km/s since the acceleration strongly increases due to the rapid reduction in mass (in fact, when $R_d \to 0$ and $T_d > T_{sub}$, one obtains $dv_d/dt \approx F_{ion,i}/M_d \propto 1/R_d$). Velocity components change abruptly during collisions with material surfaces, so that the dominant toroidal velocity component can be transformed into the poloidal components.

As discussed in Ref. [30], dust particles levitating inside the plasma sheath nearby divertor plates can accelerate to 10 m/s along the magnetic field and leave the sheath region due to diffuse collisions with the corrugated surface arising from erosion and re-deposition. For simplicity, we do not simulate dust behavior inside the sheath; instead, we specify the v_{d0}, μ_{d0} and employ reflection boundary conditions. The impact of the initial velocity value on dust particle trajectory is highlighted in Fig. 3. The upper panel displays four trajectories calculated for DIII-D shot 1055017. All trajectories originate from the same point chosen near the separatrix strike point at the outer divertor plate. The particles of radius r_{d0}=10 μm are launched at angle $\mu_{d0}=30^o$ from normal. The trajectories correspond to the following values of initial velocity v_{d0}: 10^1(A), 10^2(B), 10^3(C), 10^4(D) cm/s. As seen, for large $v_{d0} \geq 10^4$cm/s the trajectory (D) is almost a straight line from plate

to core, whereas for smaller v_{d0} the trajectories depend largely on $\mathbf{F}_d$. Strictly, Fig. 3 displays the {r,z} traces of each trajectory. The traces have different wall collision points as well as turning points. Toroidal curvature impacts the dust particle dynamics as can be seen, for example, from the trace of trajectory B. Here the particle is reflected at a point on the vertical part of outer divertor plate, and then moves on a nearly straight line until it collides with the outboard chamber wall. The corresponding trace of line segment exhibits the turning point near the separatrix leg. The line is approximately tangential to the circumference in {r,θ} with radius corresponding to the turning point.

For each trajectory in Fig. 3 (middle and bottom panels), we also show the variation of M_d and T_d along the trajectory (i.e. versus $L_p/L_{p,max}$). Because divertor plasma is strongly inhomogeneous, the trajectories have different relative variations of mass and temperature. However, the trajectories have many common features, e.g. trajectory elongation in the toroidal direction, fast acceleration of particle up to hundreds m/s by plasma flow near the plate, as well as intensive heating and enhanced loss of mass due to sublimation when the particle passes through hot plasma regions.

Dynamics of dust particles depend strongly on the reflectivity from material surfaces. We calculate trajectories for the NSTX shot considered previously using different model assumptions for dust-material interaction. We launch the particles at inner strike point, v_{d0}=10 m/s, $\mu_{d0}=30^o$, r_{d0}=1 μm and consider two cases with different reflectivities: high $[P_{ref,m}]^3$=0.95 (case 1) and low $[P_{ref,m}]^3$=0.45 (case 2). The corresponding trajectories are shown on top left panel in Fig. 4. The temporal evolution curves are displayed for the

dust radius (top right panel), velocity (bottom right), and vertical coordinate z (bottom left). The collision events are clearly seen on the radius evolution curve, they result in steps at which the radius drops by $P_{ref,m}$. In both cases, the particle experiences several collisions with divertor plate at the very beginning of the trajectory. Moreover, the number of collisions with plate can increase with decreasing reflection coefficient. The particle moves from the inner divertor far into the outer divertor in case 1, whereas in the case 2 the trajectory is localized in the inner divertor. If reflectivity is small (case 2), the dust radius rapidly decreases an e-fold in a few ms (top right) and the particle evaporates much closer to the divertor plate (left bottom). The simulation also shows that particles with smaller reflectivity $[P_{ref,m}]^3=0.1$ do not survive such a series of collisions and lost their mass in the divertor not far from the birth point (the case is not shown).

IV. Trajectories of dust particles in ITER

We use UEDGE to obtain the profiles of plasma parameters and flows for the ITER project. The calculations are done for D/T burning plasma case based on 114 MW power input to the SOL. DUSTT is then used to calculate the dust particle trajectories.

In Fig. 5, three trajectories are displayed for $v_{d0}=10^2$ (A), 10^3 (B), and 10^4 (C) cm/s calculated for $r_{d0}=1$ μm (upper panel) and $r_{d0}=10$ μm (bottom panel). All trajectories originate from the strike point at the inner divertor plate, and the sample particles are emitted at almost normal direction $\mu_{d0}=10^o$. Because of large heat flux to the dust surface, these particles are mostly burned up due to sublimation within the divertor plasma. The

variation of the dust particle mass along the trajectory is given in the right panels. Some dust particles provide significant impurity neutral sources near the core. The particle size plays a crucial role in the dust dynamics. The larger the radius, the longer is the dust lifetime with more extensive penetration into the plasma. Such penetration results in more dust mass delivered closer to the X-point, as it shown from comparison between 1- and 10- μm trajectories (top and bottom panels). The change in impurity density profiles from such sources may have strong effect on divertor plasma parameters, plasma radiation, and power loads on the divertor plates.

The trajectories originating from the top of the ITER private-flux dome are shown on Fig. 6 (upper left panel) for r_{d0}=1 μm and v_{d0}=10^2 (A), 10^3 (B), and 10^4 (C). The corresponding variation of dust temperature and mass along the trajectory are displayed in the left panels. As seen, even 1-μm particles from this location can efficiently penetrate toward the X-point. Because of strong radial gradients of plasma density and temperature in the private flux region, the dust mass decreases sharply due to sublimation only when particles get close the X-point at the end of the trajectory (right panels). The total and poloidal lengths traveled by the particle (C) versus time are shown on Fig. 6, bottom left panel. This particle travels a long distance, L_t≈2 m, in about 10 ms. Near the X-point, the particle is well entertained by the plasma flow, and thus mostly moves in the toroidal direction, L_t/L_p≈5 because of small ratio of poloidal to toroidal magnetic field in this region.

In Fig. 7 we present the trajectories for particles with $v_{d0}=10^2$(A), 10^3(B), 10^4(C) cm/s, $\mu_{d0}=10^o$, $r_{d0}=1$ μm, originating from the chamber wall at the inner (left panel) and outer (right) mid-planes. All particles penetrate radially through the SOL to the separatrix (the location of separatrix can be determined inspecting the UEDGE mesh; the radial mesh spacing is reduced around the separatrix). The penetration of low-v_{d0} particles in the radial direction is more efficient (i.e. more mass is delivered to the separatrix) on the inner side than on the outer side of the chamber. The effect of toroidal curvature is the possible explanation for this behavior. In fact, the plasma flows of ~10 km/s at the mid-plane are mostly in the toroidal (θ) direction. Due to the friction force, dust particles (A,B) are largely entrained by the plasma flow, and the resulting centrifugal force pushes the particle toward the core on the inboard side and toward the wall on the outboard side. Thus, the particles can gain large radial velocities and penetrate closer to the separatrix on the inboard side, whereas they have more wall collisions on the outboard side.

V. Estimates of the effect of dust particles on divertor plasma profiles

Dust particles are capable of penetrating much farther into plasma in comparison to single impurity atoms and ions. In order to estimate the effect of enhanced penetration of impurities due to dust evaporation on divertor plasma, we perform a series of UEDGE simulations for the discharges considered in which we scan the parameters that affect the impurity atom transport. UEDGE incorporates the simple diffusive gas model with coefficient $D_{imp}=2T_{imp}/[m_{imp}\nu_{imp}]$, where $m_{imp},T_{imp},\nu_{imp}$ are the mass, temperature, and collision frequency, and $T_{imp}=\alpha T_c+(1-\alpha)T_i\eta$ is a fitting parameter. Normally, as in Ref.

[4], we use α=0.95, η=0.9, $T_c \approx 0.1$ eV that gives T_{imp}=0.2-0.6 eV near material surfaces which is roughly in the energy range for sputtered particles or dissociation products.

The results of multi-fluid modeling for DIII-D shot 105517 discussed in Ref. [4] are presented in Fig. 8. The figure displays four contour plots for plasma temperature T_e (top panels) and C^+-ion density (bottom panels). The profiles are shown on Fig. 8 for two cases: α=0.99 (left panel) and α=0.8 (right), in which D_{imp} differs by ≈30 times. These are RGB color plots with red being the highest value of and blue is the lowest. Both temperature contours are plotted using the same colors for T_e values. The highest temperatures 70-200 eV are in the core region and this region is dark (red) in the upper plots. The dark region extends along divertor legs to the divertor strike points. Surrounding plasma is few eV and this region is much lighter (green). As seen (top left), for α=0.99, both inner and outer divertors are attached and the temperature $T_{e,X,in}$ attained at the inner strike point is rather high (≈7eV). The reduction of α to 0.8 results in substantial (~3x) reduction in T_e in both divertors and even causes detachment of the inner leg. In the top right plot, there is another dark (blue) region adjacent to the plate corresponding to the recombining plasma, $T_{e,X,in}$<1eV, and separated from the hot plasma torque. The contour plots of C^+ ion density on bottom panels have a large dark (blue) region corresponding to very low density. The singly ionized carbon is observed near material surfaces as light color (green) region. The improved penetration of impurity neutrals changes the C^+ density profile (bottom right) by moving it closer toward the core plasma. The C^+ concentration in the detached plasma is much higher than in the attached case. As seen on the bottom right plot, there are dark (red) regions around strike points

which have the highest concentration of C^+ ions. The concentrations of impurity ions near the separatrix are by 2-3 orders of magnitude larger in the case α=0.8 than in the low penetration case α=0.99.

VI. Conclusions

The development of a physical model for dust transport simulation and the DUSTT code has been described. The DUSTT code incorporates both dust dynamics due to comprehensive dust-plasma interactions as well as the effects of dust heating, charging, erosion, and evaporation.

Our simulations of carbon dust dynamics in the realistic tokamak plasma environment with the DUSTT and UEDGE codes show that dust particles are very mobile, penetrate deeply into the plasma, have relatively long lifetimes (~10 ms for 1-μm particles), accelerate to large velocities mainly due to the ion friction force (mean speed >100 m/s), and heat to sublimation temperatures when passing through hot plasma regions. We have shown that DUSTT is capable of reproducing important features of recent dust-related experiments in current tokamaks. Moreover, our simulation of dust transport illustrates the high mobility and possible deep penetration of dust particles toward the plasma core under ITER tokamak-reactor plasma conditions.

Future work should include generalized transport and interaction physics for improvement of DUSTT and self-consistent coupling of it to UEDGE. The dedicated experiments on 3D imaging of dust particles in tokamaks are required in order to validate the DUSTT physical models in detail. The code could then be used with more confidence for experimental data analysis and for development of predictive capability for ITER in which the dust production rate is expected to be substantially larger than in current tokamaks.

The evaporation of dust can produce a potentially large impurity ion source near the core plasma. As follows from our UEDGE simulations, if dust transport causes enhanced penetration of impurity neutrals into plasma, this can substantially decrease the divertor temperature, increase core contamination with impurities, and even strongly detach the inner divertor leg plasma.

Our results motivate more detailed experimental and theoretical studies of dust production, dynamics, charging, ablation, and transport. The coupled DUSTT/UEDGE codes are viewed as a part of an integrated model describing the plasma-material interactions and multi-species plasma transport as well as the tokamak reactor operation safety and environmental impact.

Acknowledgements

The work of Prof. Tanaka (Kanazawa University, Japan) on the DUSTT code improvement and validation during his visit to UCSD according to US-Japan Collaborative Program is gratefully acknowledged. The authors are grateful to Prof. I. Hutchinson (MIT) for discussions and providing analytical expressions for ion/dust friction force based on PIC calculations. The work was performed under auspices of the U.S. Department of Energy by UCSD under grant No. DE-FG02-04ER54739 and by University California LLNL under contract No. W-7405-Eng-48.

References

[1] R.L. Merlino, J.A.Goree, Physics Today, p.32 (July, 2004)

[2] V.E. Fortov, Physica Scripta **T107**, 90 (2004)

[3] P.K. Shukla, Phys. Plasmas **8**, 1791 (2001) ; D.A. Mendis, Plasma Sources Sci. Technology **11**, A219 (2002)

[4] V.N. Tsytovich, G.E. Morfill, H. Thomas, Plasma Physics Reports **29**, 1 (2003); **28**, 623 (2002)

[5] J. Winter, Plasma Phys. Controlled Fusion **46**, B583 (2004); Physics of Plasmas 7, 3862 (2000); Journal of Nuclear Materials **266-269**, 228 (1999)

[6] J.P. Sharpe, P.W. Humrickhouse, C.H. Skinner, et al., Journal of Nuclear Materials **337-339**, 1000 (2005)

[7] J.P. Sharpe, D.A. Petti, Fusion Engineering and Design **63-64**, 153 (2002); J.P. Sharpe, V. Rohde, A. Sagara, et al., Journal of Nuclear Materials **313-316**, 455 (2003);

[8] W.J. Carmack, K.A.McCarthy, D.A. Petti, et al., Fusion Engineering and Design **39-40**, 477 (1998)

[9] W.J. Carmack, R.A. Anderl, R.J. Pawelko, et al., Fusion Engineering and Design **51-52**, 482 (2000)

[10] A.T. Peacock, P. Andrew, P. Cetier, et al., Journal of Nuclear Materials **266-269**, 423 (1999); P. Chappuis, E. Tsitrone, M. Mayne, et al., Journal of Nuclear Materials **290-293**, 245 (2001); P.V. Romanov, B.N. Kolbasov, A. Kh. Alimov, et al., Journal of Nuclear Materials **307-311**, 1294 (2002)

[11] K.A.McCarthy, D.A. Petti, W.J. Carmack, G.R. Smolik, Fusion Engineering and Design **39-40**, 45 (1998); W.J. Carmack, G.R. Smolik, R.A. Anderi, et al., Fusion Technology **34**, 2 (1998)

[12] D.H.J. Goodall, Journal of Nuclear Materials **111-112**, 11 (1982); R.J. Maqueda, G.A. Wurden, Nuclear Fusion **39**, 629 (1999)

[13] G.F. Counsell , private communication (2004)

[14] K. Narihara, K. Toi, Y. Hamada, K. Yamauchi, et al., Nuclear Fusion **37**, 1177 (1997)

[15] P. W. West (General Atomics), submitted to PPCF (2005)

[16] T. Hirai, S. Brezinsek, W. Kuehnlien, et al., Physica Scripta **T111**, 163 (2004); M. Rubel, M. Cecconello, J.A. Malmberg, et al., Nucl Fusion **41**, 1087 (2002); Y. Koza, E. Berthe, E. Lehmann, et al., J. Nucl. Materials **329-333**, 706 (2004)

[17] V.T. Astrelin, A.V. Burdakov, P.Z. Chebotarev, et al., Nucl. Fusion **11**, 1541 (1997); A.T. Ramsey, C.E. Bush, H.F. Dylla, et al., Nucl. Fusion **31**, 1811 (1991); D. Pasini et al., J. Nucl. Materials **176-177**, 186 (1990); J.P. Sharpe, M. Bourham, J.G. Gilligan, Fusion Technology 34, 634 (1998)

[18] G. Y. Antar (UCSD), private communication (2005)

[19] T. Kunugi, Y. Seki, J. Fusion Energy **16**, 181 (1997); K. Masaki, K. Sugiyama, T. Hayachi, et al., J. Nucl. Materials **337-339**, 553 (2005)

[20] G.F. Federichi, C.H. Skinner, J.N. Brooks, et al., Nucl. Fusion **41**, 1967 (2002)

[21] K. Koga, R. Uehara, Y. kitaura, et al., IEEE Transactions on Plasma Science **32**, 405 (2004); J. Linke et al., Fusion Eng. Design **66-68**, 395 (2003); H. Wurz, B. Bazylev, I. Landmann, S. Pestchanyi, V. Safronov, J. Nucl. Materials **307-311**, 60 (2002)

[22] C. Arnas, C. Dominique, P. Roubin, et al., J. Nucl. Materials **337-339**, 69 (2005); A. Garscadden et al., Plasma Source Sci. Technol. **3**, 239 (1994); G.M. Jellum, D.B. Graves, J. Appl. Phys. **67**, 6490 (1990)

[23] P. Wienhold, V. Philipps, A. Kirschner, et al., J. Nucl. Materials **313-316**, 311 (2003)

[24] T. Hino, H. Yoshida, Y. Yamauchi, et al., Fusion Eng. Design **61-62**, 605 (2002); H. Yoshida et al., Fusion Sci. Technol. **41**, 943 (2002)

[25] G. Janeschitz, J. Nucl. Materials **290-293**, 1 (2001)

[26] G. Federici, J.P. Coad, A.A. Haasz, et al., J. Nucl. Materials **283-287**, 110 (2000)

[27] N.P. Taylor, Fusion Sci. Technol. **47**, 959 (2005); D.A. Petti, Fusion Sci. Technol. **47**, 967 (2005); S.J. Piet, L.N. Topilski, H-W. Bartels, et al., Fusion Eng Design **42**, 21 (1998); S.J. Piet, L. DiPace, G. Federici, J. Fusion Energy **16**, 11 (1997)

[28] Y. Oda, T. Nakata, T. Yamamoto, et al., J. Fusion Energy **16**, 231 (1997)

[29] C. Gordon, W. Gulden, B. Kolbasov, D. Petti, K. Takase, Fusion Eng. Design **55**, 347 (2001)

[30] S.I. Krasheninnikov, Y. Tomita, R.D. Smirnov, R.K. Janev, Physics of Plasmas **11**, 3141 (2004)

[31] J.D. Martin, M. Coppins, G.F. Counsell, J. Nucl. Materials **337-339**, 114 (2005)

[32] A.V. Ivlev et al., Phys. Review E **71**, 016405 (2005); S.A. Khrapak, A.V. Ivlev, G.E. Morfill, Phys. Review E **70**,056405 (2004)

[33] I.H. Hutchinson, Plasma Phys. Control. Fusion **47**, 71 (2005); **45**, 1477 (2003); **44**, 1953 (2002)

[34] S.I. Krasheninnikov, T.K. Soboleva, Plasma Phys. Control. Fusion **47**, A339 (2005)

[35] P.S. Krstic, D.J. Dean, X.-G. Zhang, et al., Computational Materials Sci. **28**, 321 (2003); E. Apra, E.J. Bylaska, D.J. Dean, et al., Computational Materials Sci. **28**, 209 (2003)

[36] G. Federici, A. Loarte, G. Strohmayer, Plasma Phys. Control. Fusion **45**, 1523 (2003)

[37] D. Stull, H. Prophet, *JANAF Thermochemical Tables* (National Bureau of Standards, Washington D.C., 1971); C.L. Mantell, *Carbon and Graphite Handbook* (Interscience Pub. New York, 1968) p.538; B.T. Kelly, *Physics of Graphite* (Applied Science Pub., London, 1981) p.477

[38] N. Razor, J. McJelland, J. Phys. Chem. Solids **15**, 17 (1960)

[39] C.A. Klein, M.J. Berry, P.A. Miles, J. Appl. Phys. **65**, 3425 (1989)

[40] H.M. Mott-Smith, I. Langmuir, Phys. Rev. **28**, 727 (1926)

[41] E.C. Whipple, Rep. Prog. Phys. **44**, 1197 (1981)

[42] E.R. Keiter, M.J. Kushner, J. Appl. Phys. **83**, 5670 (1998)

[43] P.M. Kolesnikov, *Electrodynamic acceleration of plasma* (translated from Russian), Atomizdat, Moscow, 1971.

[44] M.J. Baines, I.P. Williams, A.S. Asebiomo, Mon. Not. R. Astron. Soc. **130**, 63 (1965)

[45] S.I. Krasheninnikov, Phys. Lett. A **283**, 368 (2001); D.A. D'Ippolito, J.R. Myra, S.I. Krasheninnikov, et al., Contrib. Plasma Phys **44**, 205 (2004)

[46] G.Y. Antar, S.I. Krasheninnikov, P. Devynck, et al., Phys. Rev. Letters **87**, 065001 (2001); S. Zweben, D.P. Stotler, J.L. Terry, Phys. Plasmas **9**, 1981 (2002)

[47] J.A. Boedo, D. Rudakov, R. Moyer, et al., Phys. Plasmas **10**, 1670 (2003)

[48] A.Yu. Pigarov, S.I. Krasheninnikov, W.P. West, J. Nucl. Materials **313-316**, 1076 (2003)

[49] D. Heifetz, D. Post, M. Petravic, et al., J. Comp. Phys. **46**, 309 (1982); J. Spanier, E.M. Gelbard, *Monte Carlo Principles and Neutron Transport Problems* (Addison-Wesley Publ., Reading Massachusetts, 1969)

[50] W. Eckstein, J. Nucl. Materials **248**, 1 (1997) and literature cited therein.

[51] E.W. Thomas R.K. Janev, J.J. Smith, Nucl. Instrumental Methods B **69**, 427 (1992); R. Ito, T. Tabada, N. Itoh, IPPJ-AM-41, Institute of Plasma Physics, Nagoya, Japan (1984); T. Tabada, R. Ito, K. Morita, et al., Nucl. Instrum. Methods Phys. Res. B **9**, 113 (1985)

[52] Reflection coefficients (R) and sputtering yields (Y) depend strongly on the incident energy and angles. The coefficients/yields are given by complicated analytical expressions, so that numerical averaging of R and Y over the corresponding velocity distribution function is rather time-consuming. In the calculations, for simplicity, the simplified approach was employed. We use analytical expressions without such averaging but we substitute the effective values for incident energy and angles.

[53] W. Eckstein, R. Preuss, J. Nucl. Materials **320**, 209 (2003); C. Garcia-Rosales, W. Eckstein, J. Roth, J. Nucl. Materials **218**, 9 (1994); J. Bohdansky, Nucl. Instrumental Methods B **2**, 587 (1984); N. Matsunami, Y. Yamamura, Y. Itikawa, et al., Atomic Data Nucl. Data Tables **31**, 1 (1984)

[54] J. Roth, J. Nucl. Materials **266-269**, 51 (1999); J.W. Davis, A.A. Haasz, J. Nucl. Materials **241-243**, 37 (1997). We also used improved analytical fits for chemical yield dependence on projectile energy and incident flux given by J.D. Elder and recently

incorporated into UEDGE and DIVIMP [P.C. Stangeby, J.D. Elder, J. Nucl. Materials **220-223**, 193 (1995)] codes.

[55] J. Roth, E. Vietzke, A.A. Haasz, et al., Nucl. Fusion Supplement **1**, 63 (1991)

[56] Z. Wang, G.A. Wurden, Rev. Sci. Instrum. **74**, 1887 (2003)

[57] Yu. Martynenko (KIAE, Russia), private communication

[58] W. Eckstein, *Computer Simulation of Ion-Solid Interactions*, Springer-Verlag, NY, 1991

[59] D.A. Mendis, Astrophys. Space Sci. **65**, 5 (1979); Ann. Rev. Earth Planet. Sci. **2**, 419 (1974)

[60] T.D. Rognlien et al., J. Nucl. Materials **196-198**, 347 (1992); A.Yu. Pigarov, E.M. Hollmann, S.I. Krasheninnikov, T.D. Rognlien, J. Nucl. Materials **337-339**, 371 (2005)

[61] D.L. Rudakov (UCSD), private communication (2005)

Figure captions

Fig.1: Sample trajectories of dust particles calculated for L-mode plasma discharge 109033 on NSTX tokamak.

Fig.2: The trajectory of dust particle and corresponding evolution of dust parameters calculated for L-mode plasma discharge 105517 on DIII-D tokamak.

Fig.3: Dust particle trajectories correspondent to different values of initial dust velocities (upper panel) in DIII-D and variation of dust temperature (middle) and mass (bottom panel) along these trajectories.

Fig.4: Dust particle trajectories correspondent to different values of particle reflectivity from the PFCs in NSTX (upper left panel). Other panels display temporal evolution of dust radius, velocity, and vertical coordinate for these trajectories.

Fig.5: Trajectories of dust particles originated from the strike point at inner divertor plate in ITER are shown for initial dust radius 1 μm (upper left panel) and 10 μm (bottom left panel). Trajectories A, B and C correspond to different values of initial dust velocity. The correspondent variation of mass of these particles along the trajectory is displayed in the right panels.

Fig.6: Trajectories of dust particles originated from the private-flux dome in ITER at different initial velocities (upper left panel), variation of dust temperature and mass along these trajectories (left panels), and the temporal evolution of total (L_t) and poloidal (L_p) travel distances (bottom right).

Fig.7: Trajectories of dust particles originated from inner (left panel) and outer (right) mid-plane locations in ITER.

Fig.8: Color contour plots for simulated 2D profiles of plasma temperature (upper panels) and singly-ionized carbon density (bottom panels) in the DIII-D divertor region. Left and right contours correspond to different penetration of neutral carbon atoms.

Table 1

Characteristic of dust	NSTX	DIII-D	C-Mod
Count-based median diameter, μm	3.27(a)	0.6 (b)	1.8(c)
Diameter of average mass, μm	---	3(b)	8.4(c)
PFC surface dust-mass density, mg/m^2	6(a)	3(c,d)	100(c)
Averaged dust-mass density, mg/m^2	34 (a)	24(d)	1000(c)
Total inventory, g	0.5(a)	120(c,d)	---

(a) Ref.[6], (b) Ref.[8], (c) Ref.[9], (d) Ref.[7]

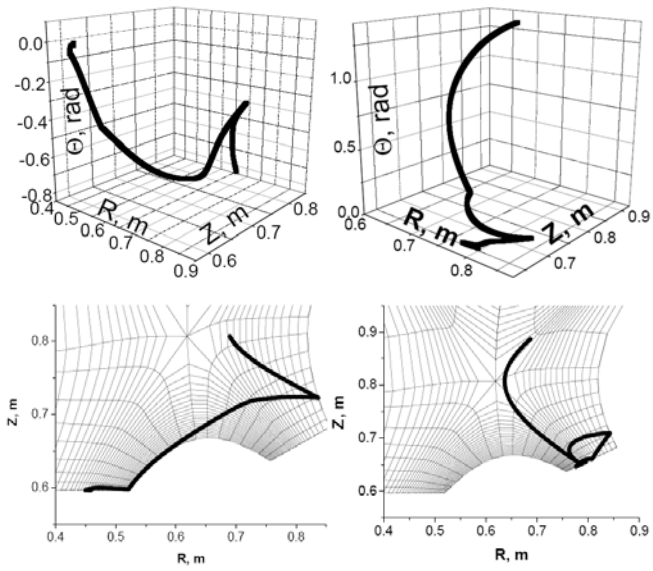

Fig. 1

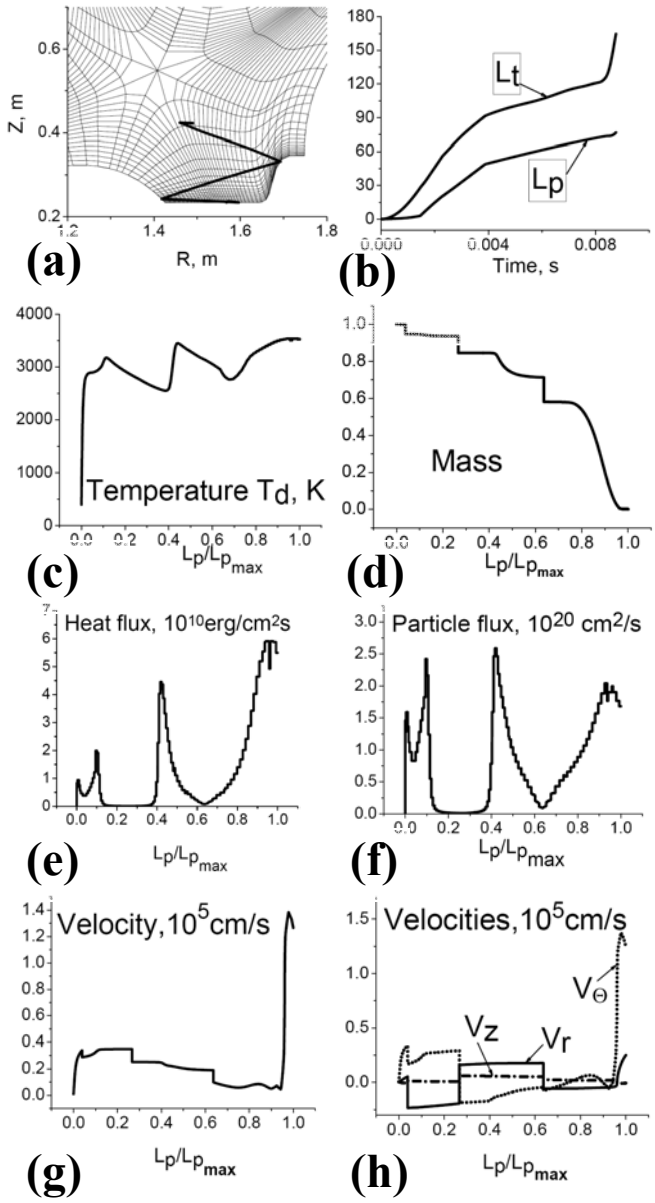
Z, m
R, m
(a)
Lt
Lp
Time, s
(b)
Temperature Td, K
Lp/Lpmax
(c)
Mass
Lp/Lpmax
(d)
Heat flux, 10¹⁰erg/cm²s
Lp/Lpmax
(e)
Particle flux, 10²⁰ cm²/s
Lp/Lpmax
(f)
Velocity,10⁵cm/s
Lp/Lpmax
(g)
Velocities,10⁵cm/s
VΘ
Vz
Vr
Lp/Lpmax
(h)

Fig.2

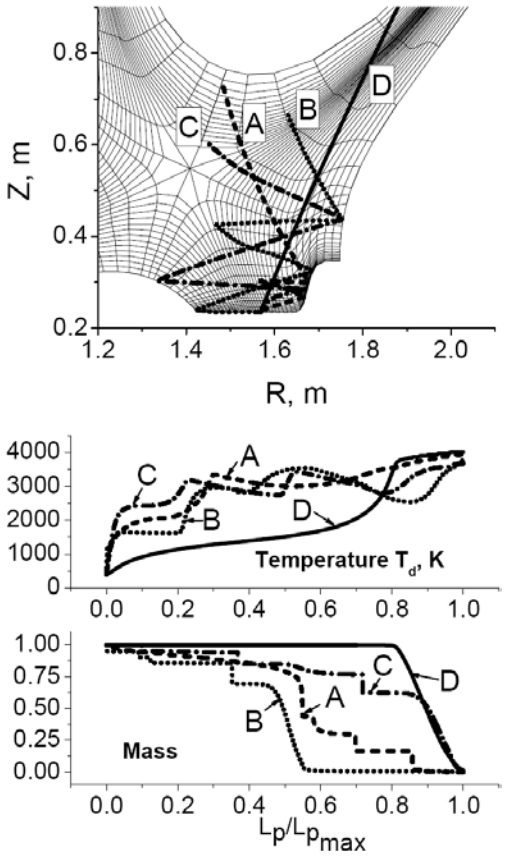

Fig. 3

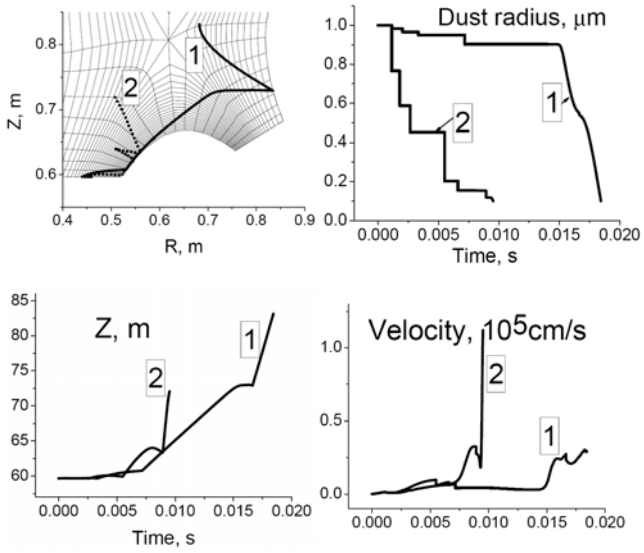

Fig. 4

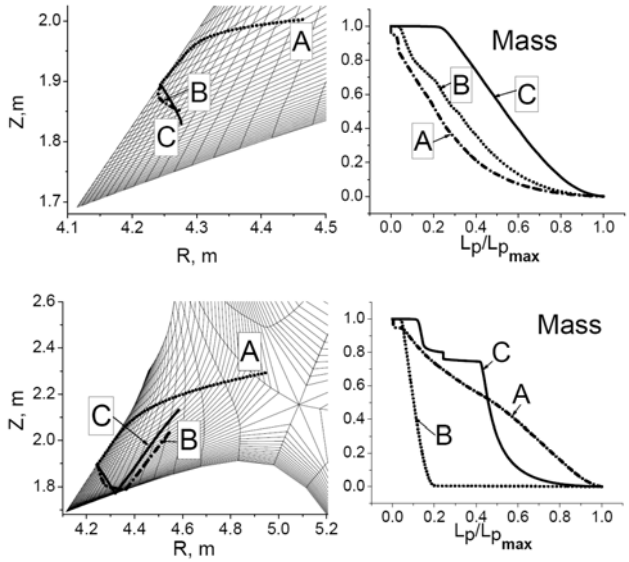

Fig.5

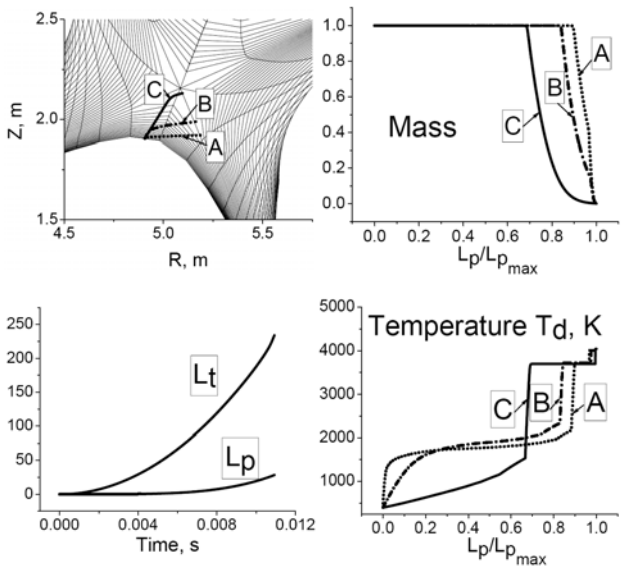

Fig. 6

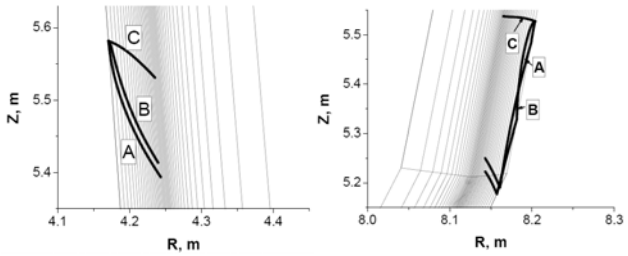

Fig. 7

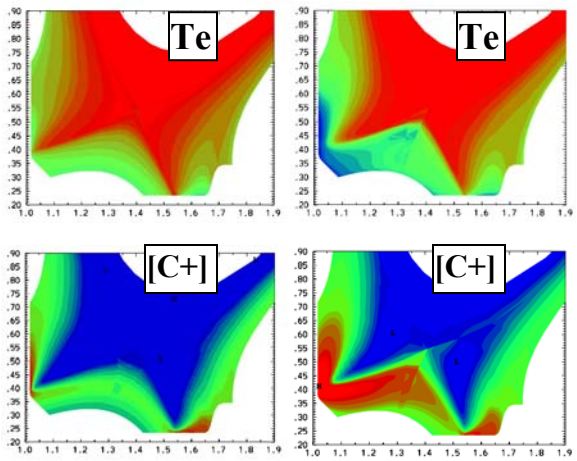

Fig. 8